

Radio emission from cosmic ray air showers: simulation results and parametrization

T. Huege^{a,*}, H. Falcke^{b,c,a}

^a*Max-Planck-Institut für Radioastronomie, Auf dem Hügel 69, 53121 Bonn, Germany*

^b*Radio Observatory, ASTRON, Dwingeloo, PO Box 2, 7990 Dwingeloo, The Netherlands*

^c*Dept. of Astronomy, University of Nijmegen, PO Box 9010, 6500 GL Nijmegen, The Netherlands*

Abstract

We have developed a sophisticated model of the radio emission from extensive air showers in the scheme of coherent geosynchrotron radiation, providing a theoretical foundation for the interpretation of experimental data from current and future experiments. Having verified the model through comparison of analytic calculations, Monte Carlo simulations and historical experimental data, we now present the results of extensive simulations performed with our Monte Carlo code. Important results are the absence of significant asymmetries in the total field strength emission pattern, the spectral dependence of the radiation, the polarization characteristics of the emission (allowing an unambiguous test of the geomagnetic emission mechanism), and the dependence of the radio emission on important air shower and observer parameters such as the shower zenith angle, the primary particle energy, the depth of the shower maximum and the observer position. An analytic parametrization incorporating the aforementioned dependences summarizes our results in a particularly useful way.

Key words: extensive air showers, radiation mechanisms, computer modeling and simulation, cosmic ray detectors

PACS: 96.40.Pq, 95.30.Gv, 95.75.-z, 95.55.Vj

* Corresponding author.

Email addresses: `thuege@mpifr-bonn.mpg.de` (T. Huege), `falcke@astron.nl` (H. Falcke).

1 Introduction

Radio emission from cosmic ray air showers, initially predicted by Askaryan [1; 2] and experimentally discovered in 1965 by Jelley et al. [3], offers the opportunity to carry out cosmic ray and neutrino research with radio measurements in the frequency range from a few to a few hundred MHz. The radio technique yields data very much complementary to those collected with ground-based particle detector arrays and air shower fluorescence detectors and incorporates the advantages of a 100% duty cycle, moderate cost per antenna, and the possibility of observation even in populated areas [4].

After the vivid activities of the 1960ies and 1970ies, research in this field virtually ceased completely in the late 1970ies due to experimental problems, difficulties in the interpretation of the experimental data and the success of alternative techniques. With the advent of new fully digital radio interferometers such as LOFAR¹ and the ideas put forward by Falcke & Gorham in [4], the radio technique, however, currently experiences its renaissance. Although the effect has been known for almost 40 years, the knowledge of the radio emission properties and their dependence on the underlying air shower parameters has been rather poor until recently [see, e.g., the discussion in 5]. To address this issue and to build the necessary foundation for the application of radio techniques to cosmic ray research, a number of experimental and theoretical efforts have started in the last few years.

On the experimental side, the LOPES project [6] develops and tests the design of a LOFAR prototype station for the measurement of cosmic ray air showers. It is going to provide experimental data that should finally pin down the absolute strength as well as the polarization properties of the radio emission very soon. Another ongoing effort is the CODALEMA experiment in France [7].

On the theoretical side, there have been calculations presented in [8] and [9]. Furthermore, we have developed our own analytical model of the radio emission from vertical cosmic ray air showers in the scheme of coherent geosynchrotron radiation in [5]. This model allowed us to gain a solid understanding of the important coherence effects that shape the radio emission. As a second step in our modeling efforts, we designed and implemented Monte Carlo simulations of the radio emission from cosmic ray air showers in the same scenario, yet with much higher precision and for arbitrary geometries [10]. The simulations are based on analytic parametrizations of the air shower characteristics and constitute a precursor to our upcoming full-fledged Monte Carlo simulations of radio emission from extensive air showers based on precise air shower

¹ <http://www.lofar.org>

modeling with CORSIKA [11].

In this article, we present the results inferred so far from the simulations performed with our code. After a short description of the underlying simulation parameters in section 2, we describe important characteristics of the radio emission in general such as the radial dependence, the spectral dependence, the curvature of the radio front and the polarization characteristics of the radiation (which play an important role in experimentally verifying the dominant emission mechanism) in section 3. We analyze the dependence of these characteristics on the associated air shower parameters such as the shower geometry (zenith and azimuth angle), the primary particle energy, the depth of the shower maximum, and the magnetic field in a qualitative way in section 4. Afterwards, we parametrize the emission's dependence on the various observer and shower parameters in a number of individual formulas for our reference shower (section 5) before generalizing the parametrizations to arbitrary shower geometries and piecing together an overall parametrization incorporating all dependences in section 6. We discuss our results in section 7 and conclude the article in section 8.

2 Simulation parameters

All simulations presented here were done with the Monte Carlo code described in [10]. In this section, we specify the simulation strategy as well as the parameters and configuration options that were used throughout this work.

Obviously, we cannot perform a true n -dimensional analysis of the parameter space in question. We therefore choose a vertical 10^{17} eV air shower as a reference and change only one of the shower parameters at a time to analyze its effect on the radio emission. This postulates that the effects introduced by changes of the different parameters are well-separable. We pay special attention in cases where this is obviously not true (e.g., primary particle energy and depth of the shower maximum).

Our reference air shower is calculated with a primary particle energy of 10^{17} eV, developing to its maximum at an atmospheric depth of 631 g cm^{-2} as originally adopted in [5]. This corresponds to a distance of ~ 4 km to the ground in case of a vertical air shower.

The following settings are kept throughout all simulations if not explicitly stated otherwise (definitions of the terms in quotation marks are given in [10]): The particle track lengths are distributed following an exponential probability distribution with mean track length of 36.7 g cm^{-2} for both electrons and positrons. The particle energies are set to follow a broken power-law distri-

bution peaking at $\gamma = 60$ as described in [5]. The magnetic field is chosen with a strength of 0.5 Gauss and an inclination of 70° , which approximately corresponds to the configuration present in central Europe. Calculations are done on a “simple grid” of 1 ns resolution with “smart trajectory sampling” enabled. “Automatic ground-bin inactivation” is used with a precision goal of 0.25% in 4 consecutive blocks of 10,000 particles each up to a maximum of 25,000,000 particles. A total of 800 bins (32 in azimuth; 25 in radius, up to a distance of 1000 m) is calculated in each simulation.

3 General characteristics

First, we present the general characteristics of the radio emission from a prototypical 10^{17} eV vertical air shower, which we take as the reference shower in this work.

3.1 Spectral dependence

In Fig. 1 we present the spectral dependence of the emission from a 10^{17} eV vertical air shower at various distances from the shower center. The spectra show a steep decline towards higher frequencies due to the coherence diminishing as the wavelengths become shorter and thus comparable to the scales present in the shower “pancake”. The field strength reaches a first interference minimum at a distance-dependent frequency. Afterwards, we see a quickly alternating series of maxima and minima that are insufficiently sampled in this calculation and therefore give rise to the unphysically seeming features at high frequencies. A realistic modeling of the emission in this incoherent regime would need a more detailed air shower model taking into account the inhomogeneities that are known to be present in the shower cascade. This cannot be achieved with the currently used analytic parametrizations of air shower properties, but will be accomplished once our code is interfaced to the air shower simulation code CORSIKA.

The higher the distance from the shower center, the steeper the spectral dependence of the emission. In other words, coherence is much better up to high distances at lower frequencies as compared with higher frequencies: while the emission is coherent to large distances of > 500 m for the 10 MHz frequency component, it already becomes incoherent at ~ 300 m for the 55 MHz frequency component.

Figure 2 shows the spectra of the same 10^{17} eV vertical air shower plotted in a νS_ν diagram, illustrating that most of the power is emitted at frequencies

around 20–30 MHz.

These two effects strongly point to low frequencies as the most promising regime for observation of cosmic ray air showers with radio techniques.

To demonstrate the differences for emission at low and high frequencies, we compare some of the results presented in the following sections for the two prototypical frequencies of 10 MHz (good coherence up to high distances as desirable for experimental measurements) and 55 MHz (frequency band used in the historical works and LOPES, cf. [6], but coherence only up to medium distances).

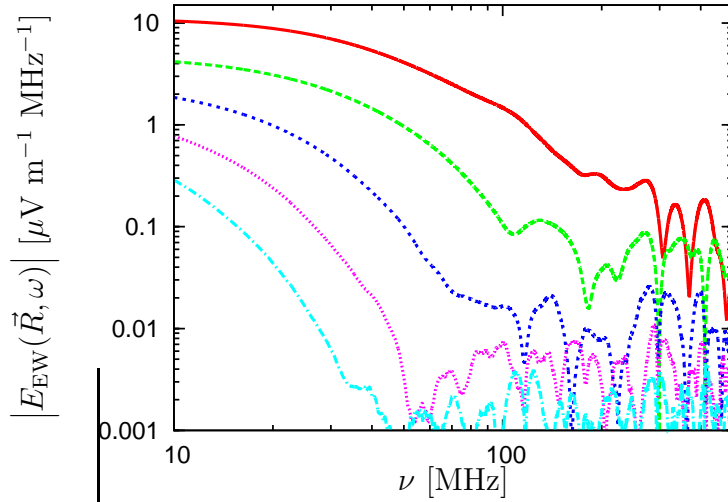


Fig. 1. Spectra of the emission from a vertical 10^{17} eV air shower at various distances to the north. From top to bottom: 20 m, 140 m, 260 m, 380 m and 500 m.

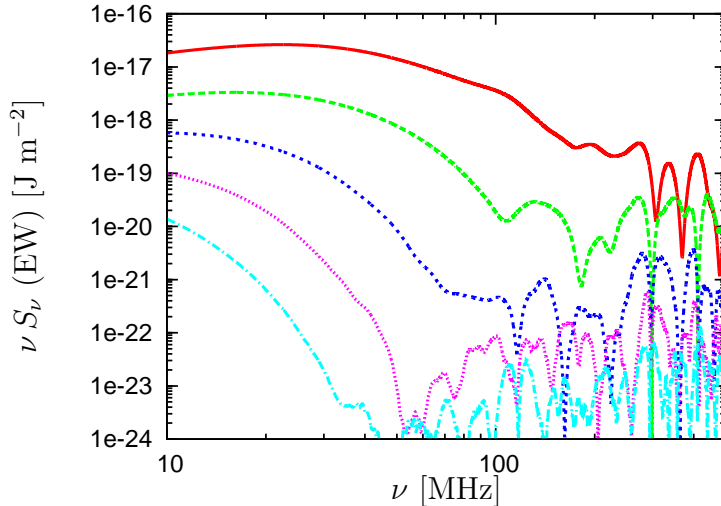


Fig. 2. Same spectra as in figure 1 plotted in a νS_ν diagram.

3.2 Radial dependence and emission pattern

Fig. 3 shows the 10 MHz component of the electric field strength in the individual linear polarization directions “north-south”, “east-west” and “vertical”. The total field strength pattern is remarkably symmetric in spite of the intrinsic asymmetry of the geomagnetic emission mechanism. A more quantitative view of the radial dependence of the emission is depicted in Fig. 4.

Please note that we can equivalently use the east-west polarization component or the total field strength in many of the following analyses as there is no flux in the north-south (let alone vertical) polarization component along the north-south direction from the shower center for air showers coming from the south.

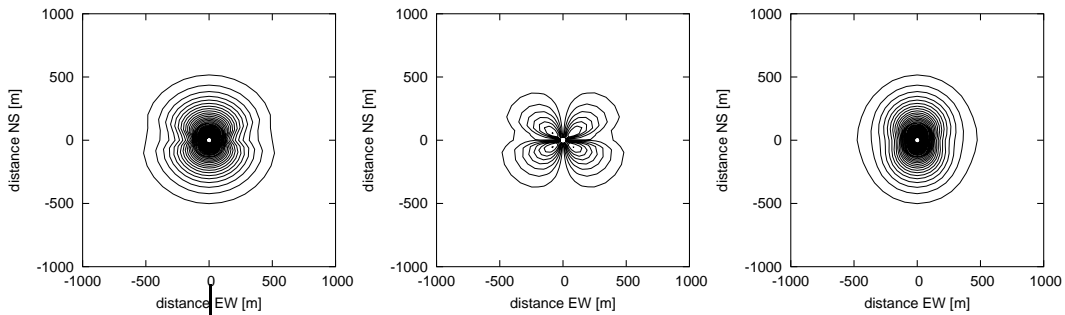


Fig. 3. Contour plots of the 10 MHz field strength for emission from a 10^{17} eV vertical air shower. From left to right: total field strength, north-south polarization component, east-west polarization component. The vertical polarization component (not shown here) does not contain any significant flux. Contour levels are $0.25 \mu\text{V m}^{-1} \text{MHz}^{-1}$ apart.

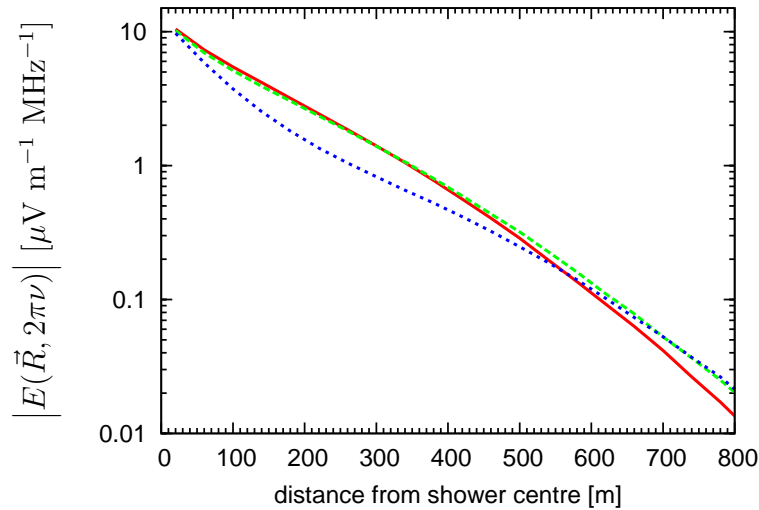


Fig. 4. Radial dependence of the 10 MHz emission from a 10^{17} eV vertical air shower. Solid: to the north, dashed: to the north-west, dotted: to the west.

3.3 Wavefront curvature

The radio wavefront arriving at the ground is not planar. As demonstrated in Fig. 5, the pulses systematically lag behind at higher distances from the shower center. The curvature of the wavefront can be approximated by a spherical surface with a given radius. At distances beyond a few hundred meters, this approximation, however, breaks down. (Additionally, the curvature radius derived from the timestamps of the maximum filtered pulse amplitudes depends on the specific filter used.) The scatter seen in the plot is not of statistical nature, but rather represents the slight time-shift in the pulses' peak amplitude as a function of azimuth angle.

The curvature of the radio wavefront plays an important role for the beamforming performed in digital radio interferometers and seems to be confirmed by LOPES measurements (Horneffer, private communication).

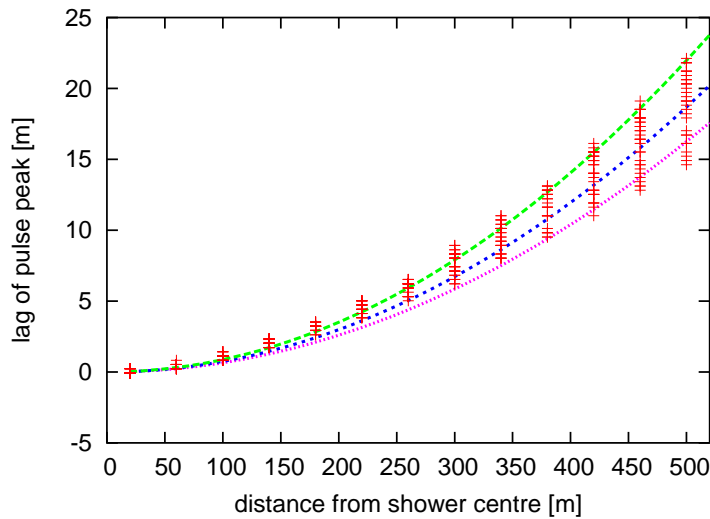


Fig. 5. Radio wavefront curvature given by the time-lag of the east-west polarization raw pulses emitted by a vertical 10^{17} eV air shower. Lines from top to bottom: curvatures given by spherical surfaces with 5,700 m, 6,700 m and 7,700 m radius.

3.4 Linear polarization

The radio emission generated by the geosynchrotron mechanism is intrinsically linearly polarized to a very high degree. Figure 6 shows the raw (unfiltered) pulses arriving at a distance of 200 m to the north-west from the center of a 10^{17} eV vertical air shower. The north-south and east-west polarization components are of similar strength and arrive almost synchronously, as expected for a linearly polarized pulse. (There is, however, also a small degree of circular polarization since the two peaks arrive not completely in coincidence.)

The vertical polarization-component is negligible.

Figure 7 shows the same data (neglecting the vertical component) visualized as a scatter plot. For each time-step of the simulated pulse, a point specifying the north-south versus east-west field strength component is drawn. In other words, the series of points directly illustrates the evolution of the (projected) electric field vector. The very narrow “loop” performed by the vector in the upper-left quadrant of the diagram demonstrates that the emission is indeed linearly polarized to a very high degree, even at the already moderate distances presented here. (In case of perfect linear polarization, the series of points would all lie on a straight line, whereas for perfect circular polarization, the polarization vector would follow a full circle around the origin.)

In the center regions where the emission is strongest, the radiation is almost perfectly linearly polarized. In these regions, the polarization vector points in the direction perpendicular to the air shower and magnetic field axes, as predicted in [5], cf. section 4.2.

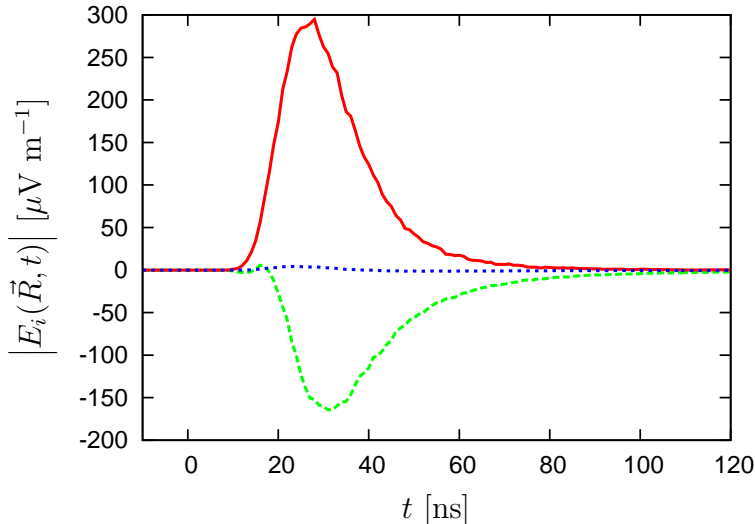


Fig. 6. Raw (unfiltered) pulses in the individual linear polarization components at 200 m distance to the north-west from the center of a 10^{17} eV vertical air shower. Solid: east-west component, dashed: north-south component, dotted: vertical component.

4 Qualitative dependence on shower parameters

In the following subsections, we present a number of dependences of the radio emission on specific air shower parameters in a qualitative way.

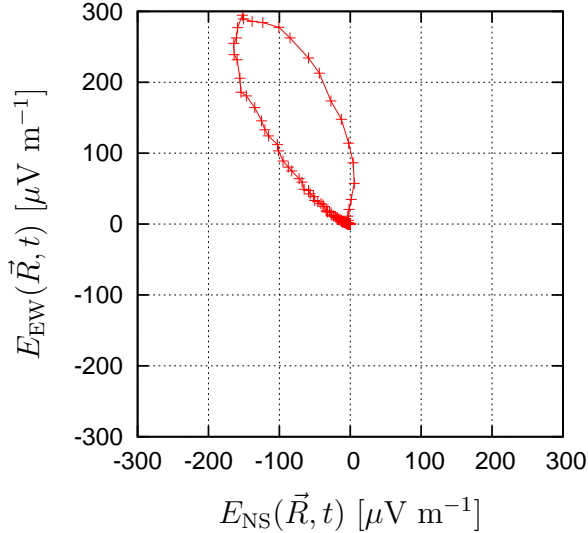


Fig. 7. Scatter plot of the north-south and east-west polarization components shown in Fig. 6. The emission is linearly polarized to a high degree.

4.1 Shower zenith angle

An interesting question is that of the radio emission’s dependence on the air shower geometry. Fig. 8 shows the radial dependence of the 10 MHz frequency component for air showers coming from the south with different zenith angles. It is well visible that the radial dependence in the north (i.e., shower axis) direction becomes much flatter with increasing zenith angle.

A broadening of the emission pattern in the shower axis direction could be intuitively expected from projection effects occurring when the air shower is inclined. One can remove these projection effects by changing the coordinate system from the ground-based “distance to the shower center” to the shower-based “(perpendicular) distance to the shower axis”. (The electric field vector, however, is still denoted with the ground-based north-south, east-west and vertical components which thus do not change in strength. This method of “back-projection” is not the same as an inclination of the full ground-plane.) Fig. 9 shows the back-projected radial dependences for the 10 MHz emission. It is obvious that the flattening is still present and thus cannot simply be caused by projection, but is an intrinsic feature of the emission. The emission pattern broadens as a whole (even in the direction perpendicular to the shower axis) as can be seen when comparing the back-projected patterns for a 45° inclined air shower depicted in Fig. 13 with that of a vertical shower shown in Fig. 3.

The overall broadening of the emission pattern is due to the fact that the air shower maximum for inclined showers is much further away from the ground than for vertical showers. This effect was already predicted from geometri-

cal/qualitative arguments by [9]. It makes inclined air showers an especially interesting target for observation with radio techniques.

The slight deviation of the 15° zenith angle curve from the trend seen in Fig. 8 is explained by the shower’s very small angle of only 5° to the 70° inclined geomagnetic field. The weakness of this deviation alone demonstrates that the dependence of the emission on the strength and orientation of the geomagnetic field is very slight — except regarding the polarization effects analyzed in Sec. 4.2. Consequently, the same diagram for air showers coming from the north (not shown here) looks very similar.

Fig. 10 shows the zenith angle dependence for the 55 MHz frequency component. The overall trend is the same as in the 10 MHz case, but the coherence losses cut off the emission pattern at a zenith angle dependent distance of a few hundred meters. At zenith angles $\gtrsim 30^\circ$, however, the coherence begins to hold up to high distances. This is confirmed by the spectra of a 45° inclined 10^{17} eV air shower shown in Fig. 11. The spectra are much flatter up to high distances when compared with the vertical case in Fig. 1.

Inclined air showers thus not only offer significantly broader emission regions on the ground, but provide the advantage that the larger “foot-print” even extends to significantly higher frequencies.

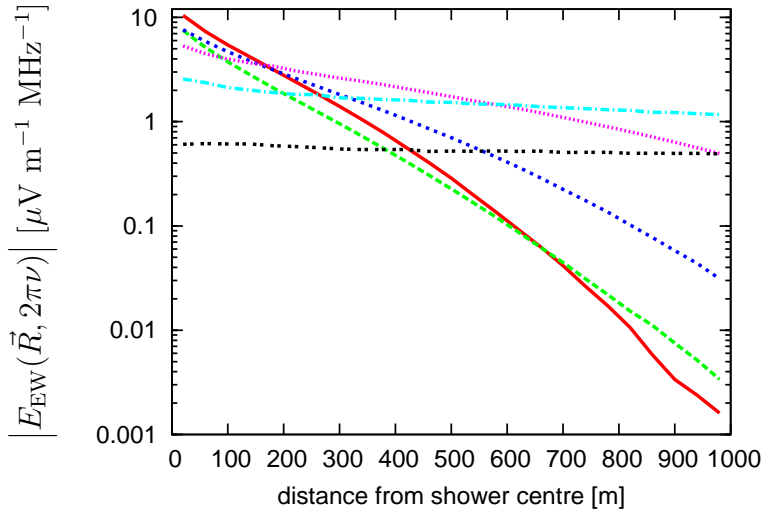


Fig. 8. Dependence of the 10 MHz east-west electric field component emitted by a 10^{17} eV air shower coming from the south for different shower zenith angles as a function of distance to the north. Red/solid: vertical shower, green/dashed: 15° , blue/dotted: 30° , violet/short dotted: 45° , turquoise/dash-dotted: 60° , black/double-dotted: 75° zenith angle.

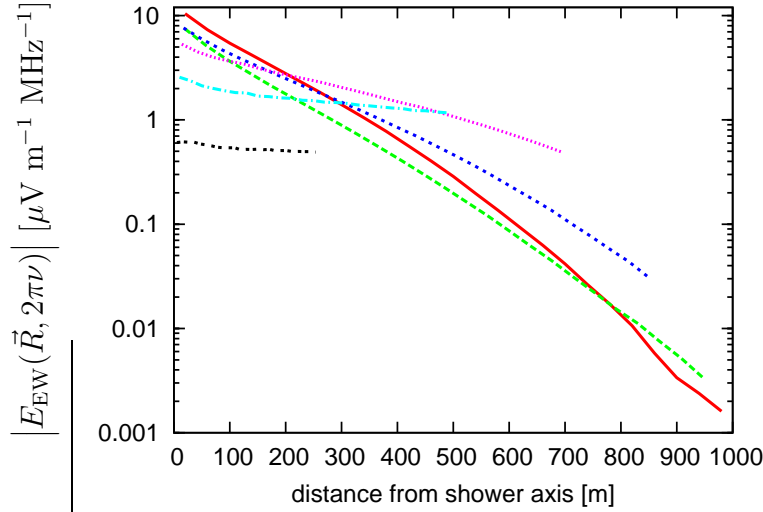


Fig. 9. Same as Fig. 8 back-projected to the shower-based coordinate system (see text).

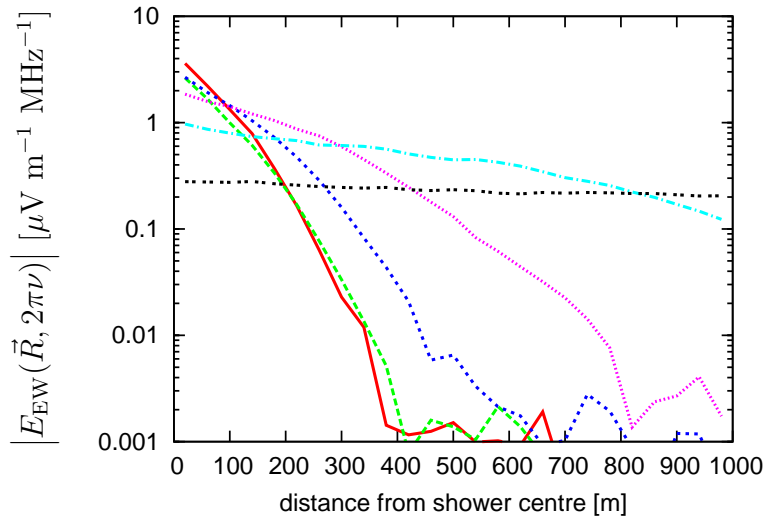


Fig. 10. Same as Fig. 8 for the 55 MHz frequency component.

4.2 Shower azimuth angle and polarization

A very important trait of the radio emission is its predicted polarization, which is directly related to the shower azimuth angle. Knowledge of this dependence is imperative for the planning and interpretation of experimental measurements.

Fig. 12 shows a comparison of the emission at 10 MHz from 10^{17} eV air showers with 45° zenith angle as a function of azimuth angle. The total field strength pattern is elongated due to the projection effects arising at high shower zenith angles (cf. section 4.1). Taking out the pure projection effects leads to the patterns depicted in Fig. 13. The patterns are much more circular, but retain

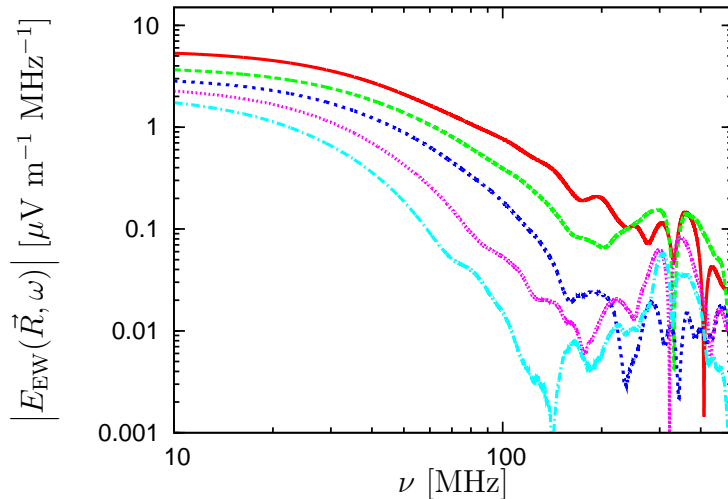


Fig. 11. Spectra of the emission from a 10^{17} eV air shower with 45° zenith angle at various distances to the north. From top to bottom: 20 m, 140 m, 260 m, 380 m and 500 m.

a significant intrinsic ellipticity and asymmetry.

The total field strength pattern of the emission (left column) simply rotates as a function of azimuth angle. (Deviations from a pure rotation are caused by the symmetry-breaking due to the magnetic field and shower axes — the emission pattern is no longer supposed to be truly symmetric.) In other words, no significant information associated to the geomagnetic field direction is present in the signal. As a direct consequence, it is not possible to verify the geomagnetic origin of the emission with an experiment measuring only the total field strength (or only one circular polarization component) of the emission. Furthermore, because the air showers arrive isotropically from all azimuthal directions, there will not be any azimuthal dependence of the measured pulse amplitudes in statistical samples of measured total field strength pulses. It will therefore not be possible to confirm air showers as the source of measured radio pulses from statistics of total field strength data alone. In this case, independent information about the simultaneous arrival of cosmic rays, e.g. from particle detectors, would be necessary.

The situation is different when one looks at the individual linear polarization components. (As demonstrated in section 3.4, the emission is polarized linearly to a very high degree.) It is visible from the right three columns of Fig. 12 that the field strength in the different polarization directions has a direct dependence on the geomagnetic field direction: the signal is linearly polarized mainly in the direction perpendicular to the air shower and magnetic field axes, at least in the central regions of high emission. The non-zero contributions in the vertical polarization direction arise from the 70° inclination of the geomagnetic field. Fig. 14 illustrates the polarization characteristics of the

central emission region in a more intuitive way through indicators denoting the ratio of north-south to east-west polarization component over-plotted over the total field strength contours.

Due to these polarization characteristics, experiments which measure the linear polarization characteristics of the emission can therefore directly verify the geomagnetic origin of the radio emission from cosmic ray air showers.

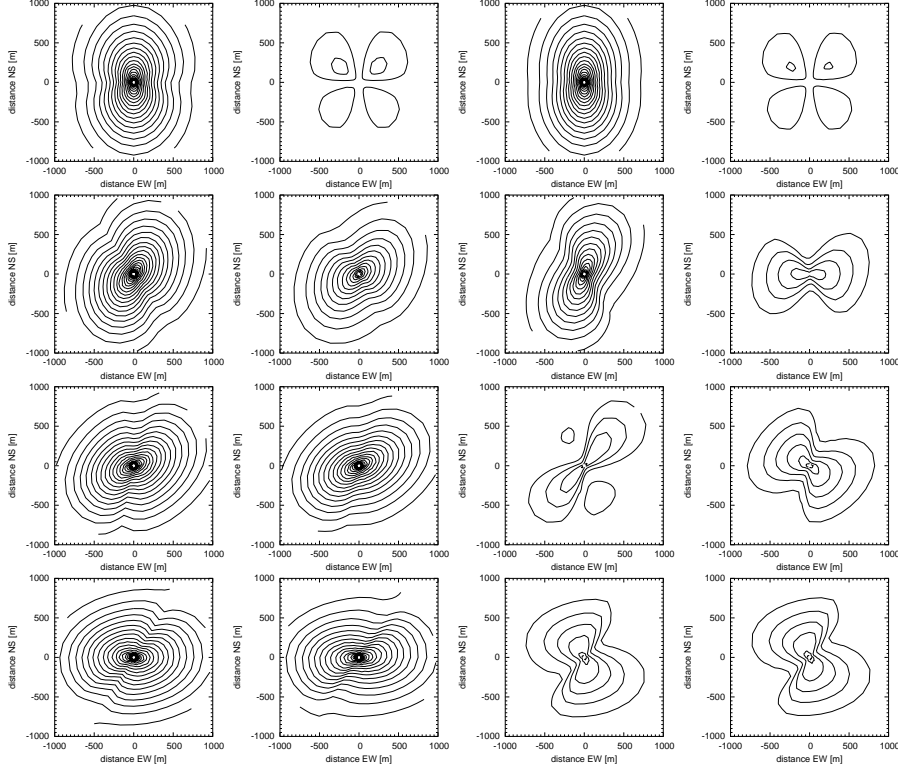


Fig. 12. Contour plots of the 10 MHz emission from a 10^{17} eV air shower with 45° zenith angle as a function of shower azimuth. Columns from left to right: total field strength, north-south, east-west and vertical polarization component. Lines from top to bottom: 0° , 30° , 60° and 90° azimuth angle. Contour levels are $0.25 \mu V m^{-1} MHz^{-1}$ apart.

4.3 Magnetic field

As discussed in section 4.2, the magnetic field has an important influence on the polarization characteristics of the radio emission. The influence on the total electric field strength, however, is very weak.

In Fig. 15 we compare the 10 MHz total field strength and polarization characteristics of vertical 10^{17} eV air showers in four different magnetic field configurations: fields of 0.3 Gauss and 0.5 Gauss strength with horizontal and 70° inclined geometry. A 0.3 Gauss horizontal magnetic field is present in the

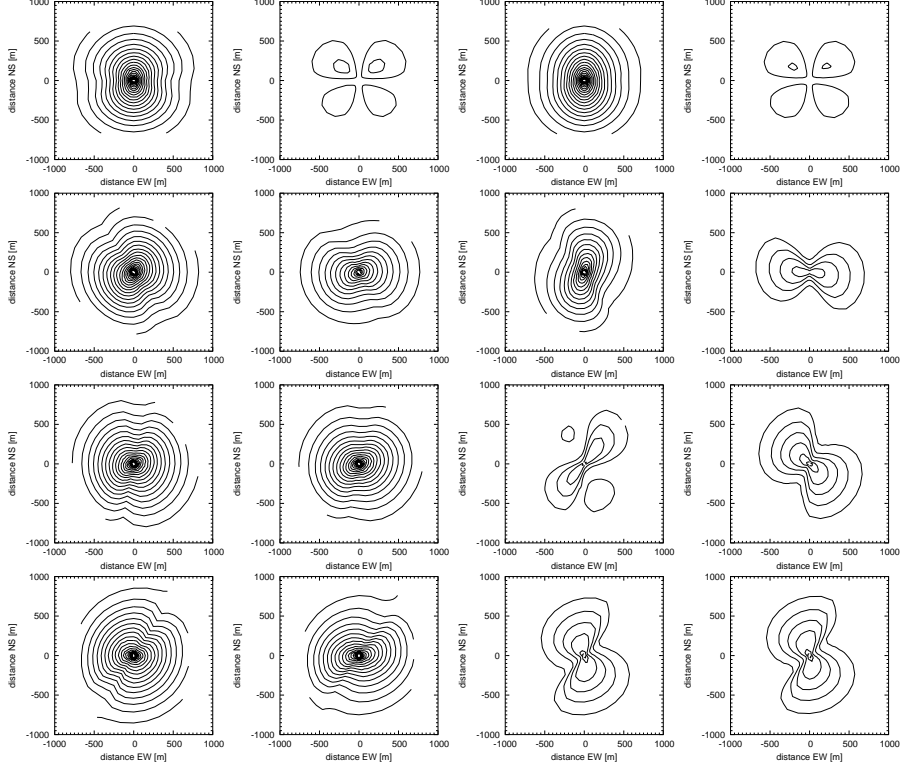


Fig. 13. Same as Fig. 12 but back-projected to the shower-based coordinate system (distances are measured perpendicularly from the shower axis).

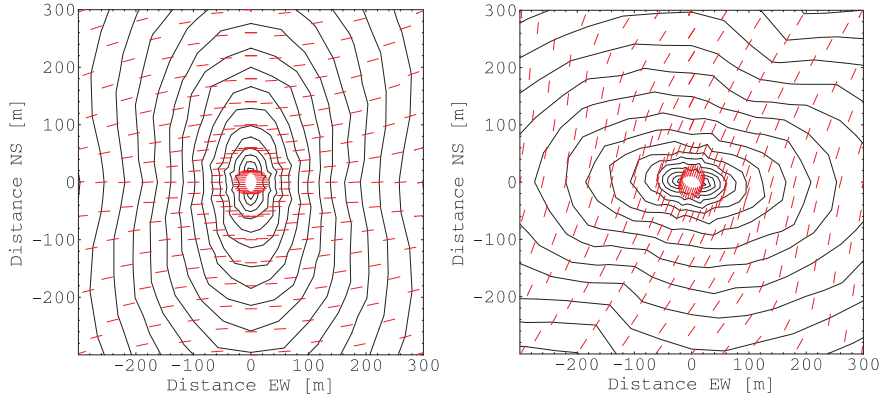


Fig. 14. Contour plot of the total 10 MHz electric field component emitted by a 10^{17} eV 45° inclined air shower with over-plotted indicators denoting the ratio of east-west to north-south polarization. Left: azimuth of 0° , right: azimuth of 90° . Contour levels are $0.25 \mu\text{V m}^{-1} \text{MHz}^{-1}$ apart.

equatorial region, whereas a $0.5 \text{ Gauss} \sim 70^\circ$ inclined magnetic field is present in central Europe.

The change from a horizontal magnetic field to a 70° inclined magnetic field introduces a number of effects. First, a small north-south asymmetry arises. Second, the overall emission level drops only very slightly — although the projected magnetic field that the vertical air shower sees drops by a factor of

$\cos^{-1}(70^\circ) \approx 3$. This demonstrates the very weak effect of the magnetic field on the total emission field strength. The most prominent change is visible in the polarization characteristics along the east-west direction from the shower center.

Increasing the field strength from 0.3 Gauss to 0.5 Gauss mainly boosts the flux in the east-west direction from the shower center in case of a horizontal magnetic field. In case of a 70° inclined magnetic field, the changes are minimal.

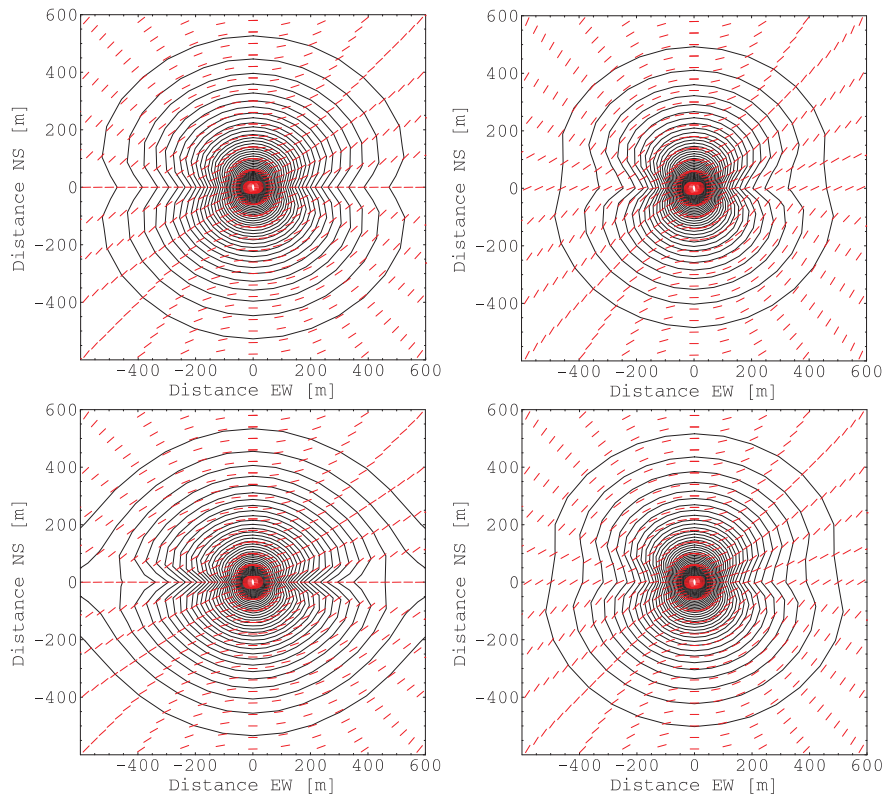


Fig. 15. Contour plots of the total 10 MHz electric field emitted by a 10^{17} eV vertical air shower with over-plotted indicators denoting the ratio of east-west to north-south polarization. Top: 0.3 Gauss magnetic field, bottom: 0.5 Gauss magnetic field, left: magnetic field horizontal, right: magnetic field 70° inclined. Contour levels are $0.25 \mu V m^{-1} MHz^{-1}$ apart.

4.4 Primary particle energy

Another important characteristic of the radio emission is its dependence on the primary particle energy. In Fig. 16 we present the dependence of the 10 MHz frequency component at various distances from the center of a vertical air shower as a function of primary particle energy. Although the depth of the shower maximum obviously depends on the primary particle energy, it is kept

constant in these calculations to assess the influence of the primary particle energy alone. (For a combined dependence see section 5.4).

The scaling of the field strength with primary particle energy is approximately linear, following a power-law $\propto E_p^{0.96}$. For 55 MHz, the diagram is very similar until the curves again cut off at distances of a few hundred meters due to coherence losses (not shown here). The spectra do not change significantly in comparison with the 10^{17} eV case except for an overall change in amplitude as demonstrated in Fig. 17 in comparison with Fig. 1.

An approximately linear scaling of the emission with primary particle energy is expected for coherent emission. In the coherent regime, the field strength directly scales with the number of emitting particles. (The emitted power consequently scales as the number of particles squared.) Since the number of particles grows approximately linearly with primary particle energy in the parametrizations at the basis of our simulations, the linear scaling directly translates to a linear scaling of the field strength with primary particle energy.

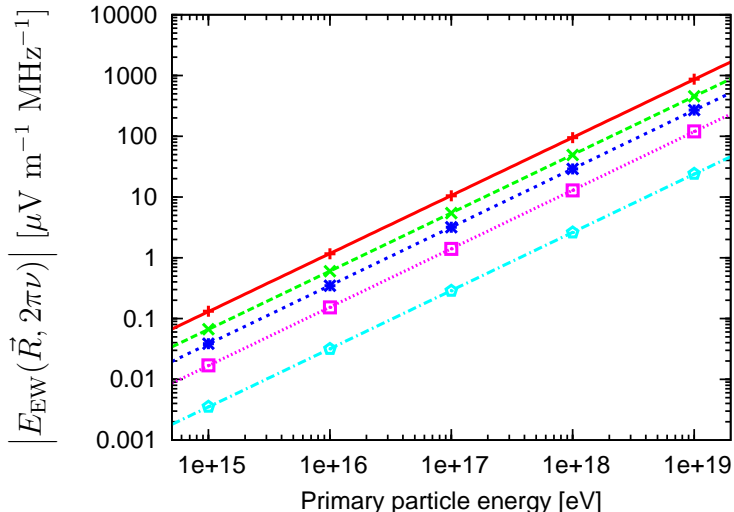


Fig. 16. Scaling of the 10 MHz east-west electric field component emitted by a vertical air shower as a function of primary particle energy E_p . From top to bottom: 20 m, 100 m, 180 m, 300 m and 500 m from the shower center. The data follow a power-law $\propto E_p^{0.96}$.

4.5 Depth of shower maximum

The depth of the air shower maximum is directly related to the nature and energy of the primary particle [cf., e.g., 12]. Additionally, it is one of the parameters that undergo strong fluctuations between individual showers with otherwise identical parameters. It is therefore interesting to evaluate the dependence of the emission on this parameter.

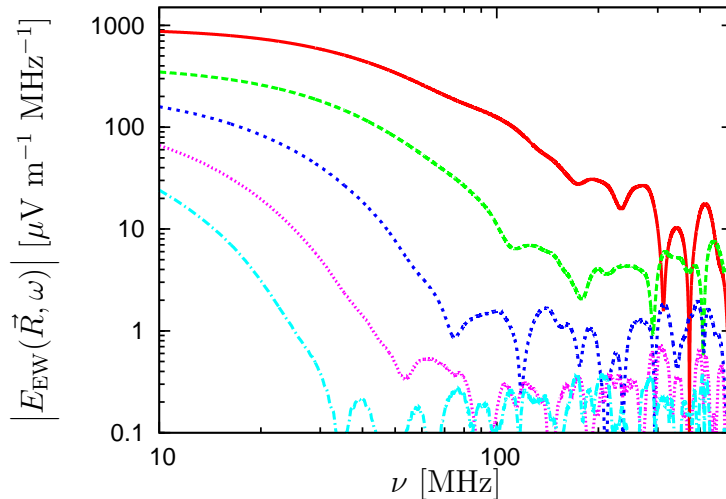


Fig. 17. Spectra of the emission from a vertical 10^{19} eV air shower at various distances to the north. From top to bottom: 20 m, 140 m, 260 m, 380 m and 500 m.

As can be seen in Fig. 18, there is a significant dependence of the emission on the depth of the air shower maximum. The deeper penetrating the air shower, the steeper becomes the radial emission pattern. This is especially important for extremely high-energy air showers $\gtrsim 10^{20}$ eV, where the shower maximum can develop close to sea-level. The effect is the same as that visible in the zenith angle dependence (cf. section 4.1), where it is much more pronounced because the (spatial) distance of the shower maximum from the ground grows very rapidly with increasing zenith angle for a given value of X_{max} .

The effect is very similar at 55 MHz, except for the cutoffs due to the loss of coherence at distances above a few hundred meters.

5 Parametrizations for vertical showers

Having analyzed the qualitative dependences of the radio emission on various air shower and observer parameters, constructing a parametrization of these dependences would be very useful. In a first step, we therefore quantify the dependences in a simple manner for vertical geometry. Afterwards, we generalize these dependences to an arbitrary geometry and piece together an overall parametrization taking into account the parameters simultaneously.

As there is no direct error estimate for the underlying Monte Carlo results, we neither specify χ^2 values nor make any error estimates for the derived fit parameters in the following sections. We specify our fit parameters with a high number of significant digits, knowing that the parameters are not determined with such high precision. Nevertheless, this allows an overall better represen-

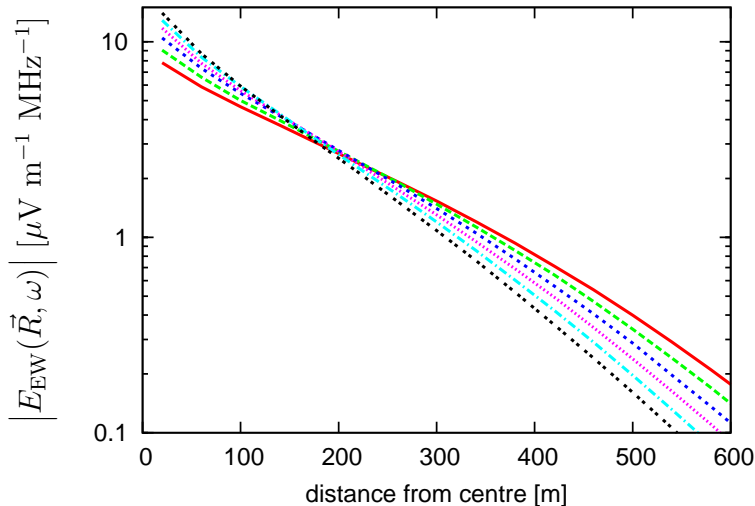


Fig. 18. Radial dependence of the 10 MHz component from a vertical 10^{17} eV air shower with various depths of the shower maximum X_{\max} . Red/solid: $X_{\max} = 560 \text{ g cm}^{-2}$, green/dashed: $X_{\max} = 595 \text{ g cm}^{-2}$, blue/dotted: $X_{\max} = 631 \text{ g cm}^{-2}$, violet/short dotted: $X_{\max} = 665 \text{ g cm}^{-2}$, turquoise/dash-dotted: $X_{\max} = 700 \text{ g cm}^{-2}$, black/double-dotted: $X_{\max} = 735 \text{ g cm}^{-2}$.

tation of the Monte Carlo results with the fit functions. To verify the quality and estimate the deviation of our parametrization from the Monte Carlo data, we then make a direct comparison of our overall parametrization and the corresponding Monte Carlo results for a sample of test parameter sets in section 6.5.

5.1 Radial dependence

The radial dependence of the emission on distance r from the shower center can be fit with an exponential decay,

$$\left| \vec{E}(r, 2\pi\nu) \right| = E_0 \exp \left[-\frac{r}{r_0} \right]. \quad (1)$$

This does not attempt to fit the behavior in the incoherent regime. Fig. 19 shows the simulated 10 MHz and 55 MHz total field strength components as a function of distance to the north from the shower center with the associated exponential fits. For the 10 MHz component, we fit one exponential in the central 500 m and a second in the outer 500 m region. This increases the quality of both fits very significantly. For the 55 MHz component, we use only the values up to 380 m, as the emission becomes incoherent at higher distances. We do not take any asymmetry of the emission pattern (cf. Fig. 3) into account in this parametrization.

ν [MHz]	E_0 [$\mu\text{V m}^{-1} \text{MHz}^{-1}$]	r_0 [m]	valid r [m]
10	12.3	135.3	0–500
10	84.4	90.44	500–1000
55	7.85	51.36	0–380

Table 1

Parameters for the radial fits according to eq. (1) depicted in Fig. 19.

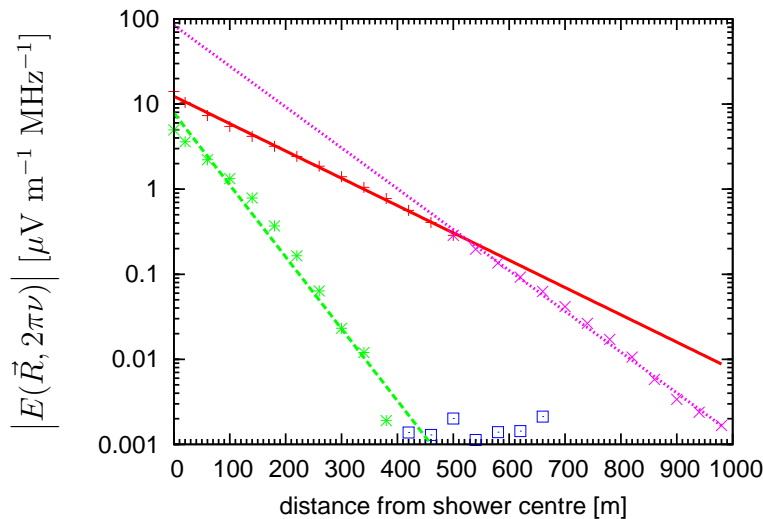


Fig. 19. Exponential radial dependence of the 10 MHz emission in the central 500 m (solid), 10 MHz emission in the outer 500 m (dotted) and 55 MHz emission (dashed) from a 10^{17} eV vertical air shower with corresponding Monte Carlo simulated data.

5.2 Spectral dependence

The spectral dependence in the coherent regime can also be parametrized well with an exponential decay. The dependence in the incoherent regime at high frequencies is not well determined by the Monte Carlo simulations performed so far. It is, however, probably flatter than an exponential decay as demonstrated from the analytical calculations, where the functional form converges towards a power-law. Outside the valid frequency-regime, the parametrization therefore is bound to underestimate the real flux. We fit the function

$$\left| \vec{E}(r, 2\pi\nu) \right| = E_0 \exp \left[-\frac{(\nu - 10 \text{ MHz})}{\nu_0} \right] \quad (2)$$

to spectra at various distances r from the shower center to the north. The parameter E_0 in this case directly represents the total field strength at 10 MHz. Only data in the coherent regime is used for the fitting procedure. The data range used is indicated in Fig. 20 together with the resulting fit functions. The associated fit parameters are listed in Table 2.

r [m]	E_0 [$\mu\text{V m}^{-1} \text{MHz}^{-1}$]	ν_0 [MHz]	valid ν [MHz]
20	10.01	46.501	10–180
140	4.693	24.382	10–110
260	1.867	14.020	10–80
380	0.7942	8.0787	10–50
500	0.2858	5.2633	10–32

Table 2

Parameters for the spectral fits according to eq. (2) depicted in Fig. 20.

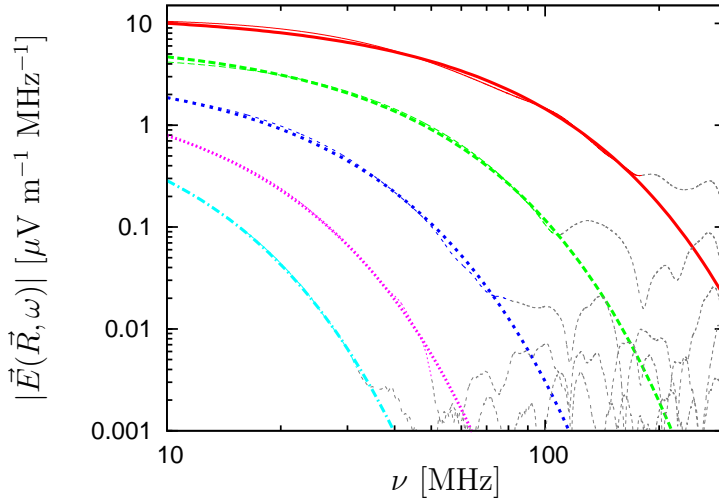


Fig. 20. Fit of exponential functions to spectra from a 10^{17} eV vertical air shower at various distances to the north. From top to bottom: 20 m, 140 m, 260 m, 380 m and 500 m. Only the data in the coherent regime is used for the fit, as indicated by the colors.

5.3 Polarization characteristics

In the center region, the emission is almost purely linearly polarized in the direction perpendicular to the magnetic field and air shower axes (cf. Fig. 14), in good agreement with the analytic calculations. In particular, the electric field vector points into the direction

$$\hat{\vec{E}}(\theta, \vartheta_B) = \frac{\begin{pmatrix} \sin \theta \sin \vartheta_B \sin \varphi \\ \cos \theta \cos \vartheta_B - \cos \varphi \sin \theta \sin \vartheta_B \\ \cos \vartheta_B \sin \theta \sin \varphi \end{pmatrix}}{\sqrt{(\cos \theta \cos \vartheta_B - \cos \varphi \sin \theta \sin \vartheta_B)^2 + \sin^2 \theta \sin^2 \varphi}}, \quad (3)$$

where θ denotes the shower zenith angle, φ is the shower azimuth angle with respect to the magnetic north and ϑ_B specifies the inclination angle (i.e., complement of the zenith angle) of the magnetic field.

Multiplication of an $|\vec{E}(r, 2\pi\nu, E_p)|$ -value with the unit polarization vector $\hat{\vec{E}}(\theta, \varphi, \vartheta_B)$ then directly yields the estimated north-south, east-west and vertical linear polarization components (in this order).

The complex dependences at higher distances from the shower center cannot be easily parametrized at this stage.

5.4 Combined E_p and X_{\max} dependence

We have discussed the radio emission's dependence on the primary particle energy and the depth of the shower maximum separately in earlier sections. Here, we parametrize the combined dependence on primary particle energy and appropriately adjusted depth of shower maximum reflecting the deeper atmospheric penetration of higher energy air showers. We set X_{\max} to 500, 560, 631, 700 and 770 g cm⁻² for E_p values of 10^{15} , 10^{16} , 10^{17} , 10^{18} and 10^{19} eV, respectively, see [12; 13]. The steepening of the radial dependence for increasing X_{\max} discussed in section 4.5 in this case leads to a radius-dependent steepening or flattening of the energy dependence (originally $\propto E_p^{0.96}$ as shown in section 4.4) in the central and outer regions, respectively. However, the combined dependence is still well-described by a power-law of the type

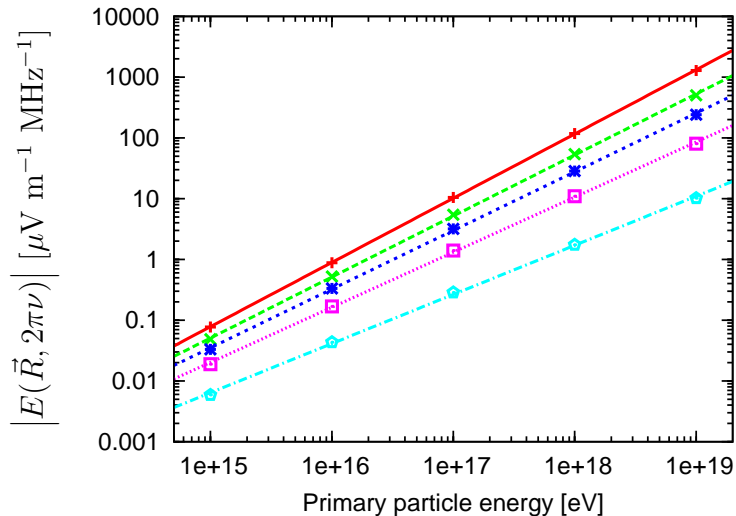


Fig. 21. Scaling of the 10 MHz electric field emitted by a vertical air shower as a function of primary particle energy E_p with appropriately changing depth of shower maximum X_{\max} . From top to bottom: 20 m, 100 m, 180 m, 300 m and 500 m to the north from the shower center.

$$|\vec{E}(r, 2\pi\nu, E_p)| = E_0 \left(\frac{E_p}{10^{17} \text{ eV}} \right)^{\kappa(r)}. \quad (4)$$

The associated fit parameters are listed in Table 3.

r [m]	E_0 [$\mu\text{V m}^{-1} \text{ MHz}^{-1}$]	κ	valid E_p [eV]
20	10.18	1.057	10^{15} – 10^{19}
100	5.188	1.004	10^{15} – 10^{19}
180	2.995	0.965	10^{15} – 10^{19}
300	1.315	0.907	10^{15} – 10^{19}
500	0.265	0.808	10^{15} – 10^{19}

Table 3

Parameters for the combined primary particle energy and depth of shower maximum dependence according to eq. (4) depicted in Fig. 21.

6 Parametrizations for arbitrary geometry

We now generalize our parametrizations of the radio emission as a function of air shower and observer parameters to an arbitrary shower geometry. As our final result, we piece the individual parametrizations together to an overall parametrization incorporating all major parameters.

6.1 Radial dependence

The emission pattern becomes increasingly asymmetric with increasing zenith angle (cf. Fig. 12). As discussed in section 4.1, most of this asymmetry is caused by projection effects that can be taken into account by changing from a ground-based coordinate system (distance r from the shower center) to a shower-based coordinate system (perpendicular distance l from the shower axis), cf. Fig. 13. The remaining intrinsic asymmetries in the emission pattern we do not take into account in our parametrization.

The back-projection from the ground-based to the shower-based coordinate system is given by

$$l(r) = r \sqrt{1 - \cos^2(\varphi_o - \varphi) \sin^2(\theta)}, \quad (5)$$

when φ and θ specify the shower azimuth and zenith angle and r and φ_o denote the observer distance from the shower center and the observer azimuth

angle (azimuth angles being measured with respect to the north). The 10 MHz back-projected radial dependence can then be well fit as

$$|\vec{E}(l)| = E_\theta \exp\left[-\frac{l}{l_\theta}\right]. \quad (6)$$

The fitting is performed as described in section 5.1 for each zenith angle θ individually. We restrain ourselves to the inner 500 m (back-projected) radius to increase the accuracy of the parametrization. We also base the fits on air showers coming from the north rather than the south to exclude the deviation for the 15° zenith angle case arising from the only 5° angle to the geomagnetic field in case of an air shower coming from the south. The resulting fits are depicted in Fig. 22, and the corresponding parameters are listed in table 4.

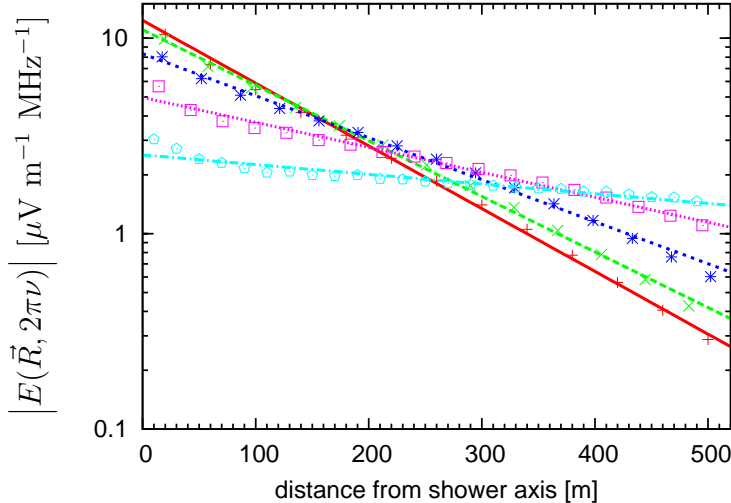


Fig. 22. Radial dependence to the north for the 10 MHz emission from a 10^{17} eV air shower with corresponding exponential fits. Red/solid: vertical shower, green/dashed: 15° , blue/dotted: 30° , violet/short dotted: 45° , turquoise/dash-dotted: 60° zenith angle.

θ	E_θ [$\mu\text{V m}^{-1} \text{MHz}^{-1}$]	l_θ [m]	valid l [m]
0°	12.33	135.30	0–500
15°	11.04	152.80	0–500
30°	8.33	202.09	0–500
45°	4.98	339.71	0–500
60°	2.53	873.54	0–500

Table 4

Parameters for the radial fits according to eq. (6) depicted in Fig. 22.

6.2 Spectral dependence

Similarly as for the radial dependence, we now generalize our parametrization for the spectral dependence of the reference shower to an arbitrary shower geometry using the same exponential fits as adopted in section 5.2. Again, for each shower zenith angle individually, we fit a number of spectra at different distances l from the shower axis using the function

$$|\vec{E}(l, 2\pi\nu)| = E_\theta(l) \exp\left[-\frac{(\nu - 10 \text{ MHz})}{\nu_\theta(l)}\right]. \quad (7)$$

We do not show the individual fits explicitly here. The resulting parameters $E_\theta(l)$ and $\nu_\theta(l)$ are tabulated in table 5. The dependence of ν_θ on the distance to the shower axis l can in turn be parametrized with an exponential function

$$\nu_\theta(l) = a_\theta e^{-l/b_\theta}. \quad (8)$$

In fact, the parameter a_θ can be fixed to the same value for all cases of θ analyzed here at only minor loss of precision. The fits with a_θ fixed to a value of 47.96 MHz are shown in Fig. 23. The associated parameters for b_θ are listed in table 6.

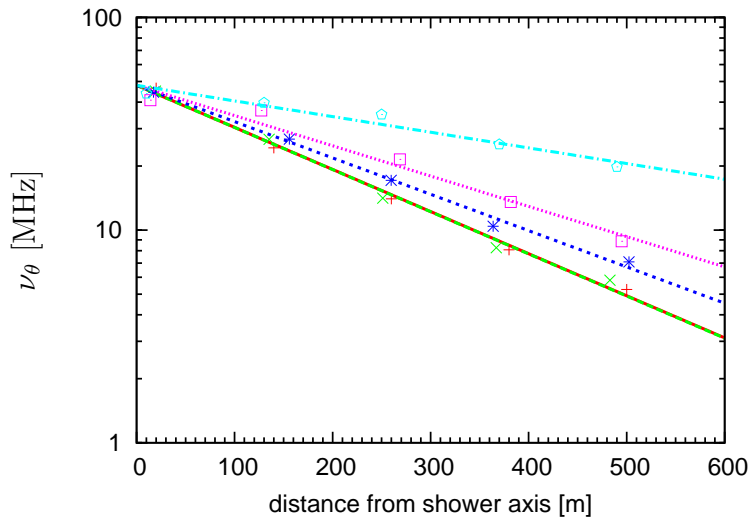


Fig. 23. Parametrization of ν_θ as a function of distance to the shower axis l according to eq. (8). Red/solid: vertical shower, green/dashed: 15° , blue/dotted: 30° , violet/short dotted: 45° , turquoise/dash-dotted: 60° zenith angle.

θ	l [m]	E_θ [$\mu\text{V m}^{-1} \text{MHz}^{-1}$]	ν_θ [MHz]	valid ν [MHz]
0°	20.0	10.01	46.501	10–180
0°	140.0	4.693	24.382	10–110
0°	260.0	1.867	14.020	10–80
0°	380.0	0.7942	8.0787	10–50
0°	500.0	0.2858	5.2633	10–32
15°	19.3	9.594	45.000	10–180
15°	135.2	4.805	26.705	10–110
15°	251.1	2.591	14.138	10–80
15°	367.1	1.183	8.2633	10–50
15°	483.0	0.433	5.8116	10–32
30°	17.3	8.185	44.532	10–110
30°	155.9	4.210	26.770	10–110
30°	259.8	2.596	17.131	10–70
30°	363.7	1.563	10.416	10–50
30°	502.3	0.582	7.0933	10–32
45°	14.1	6.145	40.824	10–110
45°	127.3	3.583	36.512	10–110
45°	212.1	2.653	21.487	10–100
45°	381.1	1.948	13.550	10–60
45°	495.0	1.245	8.866	10–50
60°	10.0	3.251	43.881	10–100
60°	130.0	2.285	39.652	10–100
60°	250.0	2.032	34.980	10–100
60°	370.0	1.964	25.318	10–80
60°	490.0	1.657	19.828	10–70

Table 5

Parameters for the spectral fits of 10^{17} eV air showers with arbitrary geometry according to eq. (7). (The arbitrary-seeming values for l are due to calculation of the air shower in the ground-based coordinate system with subsequent conversion to the shower-based coordinate system.)

θ	b_θ [m]
0°	219.41
15°	219.16
30°	254.23
45°	305.17
60°	590.03

Table 6

Parameters for the parametrization of $\nu_\theta(l)$ according to eq. (8).

6.3 Dependence of radial scale factor on X_{\max}

To factor the influence of the (vertical equivalent) depth of shower maximum into the parametrization, we have to parametrize the flattening of the emission's radial dependence with increasing X_{\max} . To achieve this, we fit the radial dependences calculated for vertical 10^{17} eV showers with various values of X_{\max} (shown in Fig. 18) with exponential functions in the central 500 m (not shown here). As can be seen in Fig. 18, the curves overlap at a distance of $l = r \sim 200$ m. Taking this point as a reference, the effect of changing X_{\max} can be reduced to a pure change of the slope, i.e., the scale factor l_θ of the exponential. We can then quantify the change of this scale factor by the ratio

$$\alpha(X_{\max}) = \frac{l_\theta(X_{\max})}{l_\theta(631 \text{ g cm}^{-2})} \quad (9)$$

of the scale factor for a given X_{\max} and the scale factor of our reference shower. Figure 24 shows α as a function of X_{\max} and a fit of this dependence using a power-law

$$\alpha(X_{\max}) = 1.00636 \left(\frac{X_{\max}}{631 \text{ g cm}^{-2}} \right)^{-1.50519}. \quad (10)$$

6.4 Overall parametrization

We now piece the individual parametrizations together to an overall formula. This implies that the different effects are independent of each other and therefore can be separated in an easy way, which need not be true in all cases. Nevertheless, such an overall parametrization can be a useful basis for comparisons of experimental data with theoretical predictions as long as one keeps the limitations of the parametrization in mind. We therefore provide a formula

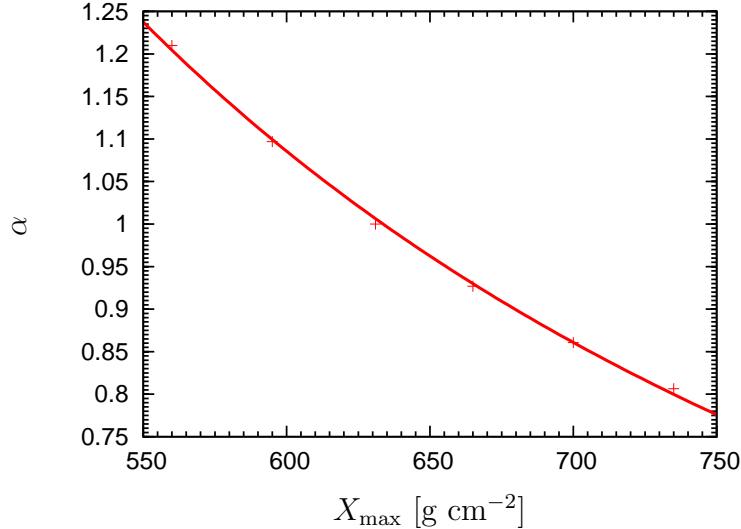


Fig. 24. Ratio α of the scale factor for a given X_{\max} to the scale factor of the reference shower as a function of X_{\max} and corresponding power-law fit.

similar to the parametrization first given by [14] and further enhanced by [4]. The associated sets of parameters are given for each zenith angle individually.

At the heart of the parametrization is the radial dependence for arbitrary geometry as described in section 6.1. This we combine with the spectral dependence derived in section 6.2 and get

$$|\vec{E}(r, \varphi_o, \nu)| = f E_\theta \exp\left[-\frac{l(r, \varphi_o)}{l_\theta}\right] \exp\left[-\frac{\nu/\text{MHz} - 10}{47.96 \exp[-l(r, \varphi_o)/b_\theta]}\right] \quad (11)$$

with the parameters as listed in table 7. The “fudge factor” f is introduced to allow deviations probable to arise in the future when a more sophisticated distribution of particle momenta (i.e., pitch-angles) is taken into account. Throughout this work, we set $f = 1$. Additionally, we can factor in the pri-

θ	E_θ [$\mu\text{V m}^{-1} \text{MHz}^{-1}$]	l_θ [m]	b_θ [m]
0°	12.33	135.30	219.41
15°	11.04	152.80	219.16
30°	8.33	202.09	254.23
45°	4.98	339.71	305.17
60°	2.53	873.54	590.03

Table 7

Parameters for the overall parametrization of the air shower emission according to eq. (12).

mary particle energy dependence (cf. 4.4) and the dependence of the radial scale factor on the (vertical shower equivalent) depth of the shower maximum

derived in section 6.3. For the latter, we have to take into account the change of the field strength in the shower center associated with the steepening of the scale factor l_θ calculated from the reference point at $l = 200$ m. The resulting overall parametrization is then given by

$$\begin{aligned}
|\vec{E}(r, \varphi_o, \nu, E_p, X_{\max})| &= f E_\theta \left(\frac{E_p}{10^{17} \text{ eV}} \right)^{0.96} \\
&\times \exp \left[-\frac{200 \text{ m} (\alpha(X_{\max}) - 1) + l(r, \varphi_o)}{\alpha(X_{\max}) l_\theta} \right] \\
&\times \exp \left[-\frac{\nu/\text{MHz} - 10}{47.96 \exp[-l(r, \varphi_o)/b_\theta]} \right] \quad (12)
\end{aligned}$$

with $\alpha(X_{\max})$ defined in eq. (10), $l(r, \varphi_o)$ given by eq. (5), the values for E_θ , l_θ and b_θ taken from table 7, and $f = 1$. To calculate the field strength for the individual linear polarization components, one can then multiply the result of eq. (12) with the unit polarization vector given in eq. (3).

6.5 Quality and validity of the overall parametrization

To verify the quality of our parametrization, we take a sample of observer parameters testing the different regimes of the parametrization and compare the result of eq. (12) with the result from the Monte Carlo simulation. As can be seen in table 8, the deviations are acceptably small: most of the time the error is below 10%, and only in cases where the parametrization is expected to degrade (e.g. in the east-west direction of heavily inclined air showers, where the intrinsic asymmetries in the emission pattern become relevant) it grows beyond 20%.

One must of course be careful not to leave the parameter regimes for which the parametrization was created. Specifically, the back-projected radial distance l was limited to 500 m in the underlying radial fits. The frequency limits for the spectral fits can be estimated from table 5 as a function of l . As explained earlier, the parametrization is bound to severely underestimate the flux at higher frequencies. The polarization characteristics given by eq. (3) are only valid for the central region as illustrated by Fig. 14. At significant zenith angles, the intrinsic asymmetries of the emission pattern which were not taken into account in the parametrization lead to a growing deviation from the Monte Carlo results. Finally, special caution should be used when changing the depth of shower maximum X_{\max} for significantly inclined air showers, as the underlying parametrization of $\alpha(X_{\max})$ was derived for vertical air showers only and the projection effects associated with inclined showers greatly enhance the depth of shower-maximum effects.

θ	E_p	X_{\max}	r	φ_o	ν	$ E_{\text{param}} $	$ E_{\text{MC}} $	deviation
[$^\circ$]	[eV]	[g cm $^{-2}$]	[m]	[$^\circ$]	[MHz]	$\left[\frac{\mu\text{V}}{\text{m MHz}}\right]$	$\left[\frac{\mu\text{V}}{\text{m MHz}}\right]$	[%]
0	10^{17}	631	0	0	10	12.22	14.07	-13.21
0	10^{17}	631	0	0	44.43	5.96	6.58	-9.51
0	10^{17}	631	100	0	10	5.86	5.45	7.47
0	10^{17}	631	420	45	10	0.56	0.59	-5.93
0	10^{17}	631	0	0	55	4.78	4.98	-4.1
0	10^{17}	560	20	0	10	8.49	7.82	8.57
0	10^{17}	735	60	0	55	2.99	2.55	17.01
0	10^{17}	735	260	0	10	1.62	1.53	5.73
0	10^{18}	700	20	0	10	120.28	118.13	1.81
0	10^{19}	631	220	45	10	172.41	199.45	-13.55
15	10^{17}	631	60	45	55	2.18	2.24	-2.42
30	10^{17}	631	100	0	55	1.45	1.59	-9.19
45	10^{17}	631	20	0	10	4.76	5.67	-16.01
45	10^{17}	631	180	0	10	3.42	3.42	0.03
60	10^{17}	631	300	0	10	2.13	1.99	6.89
60	10^{17}	631	300	45	10	1.93	2.09	-7.67
60	10^{17}	631	300	0	55	0.64	0.73	-12.59
60	10^{17}	631	300	45	55	0.47	0.66	-28.56

Table 8

Quality check of the overall parametrization given by eq. (12).

6.6 Comparison with Allan-parametrization

The authors of [14] provided a parametrization of their experimental data which has in turn been generalized by [4] to the form

$$\begin{aligned}
\epsilon_\nu = & 13 \mu\text{V m}^{-1} \text{MHz}^{-1} \left(\frac{E_p}{10^{17} \text{ eV}} \right) \left(\frac{\sin \alpha \cos \theta}{\sin 45^\circ \cos 30^\circ} \right) \\
& \times \exp \left[\frac{-r}{r_0(\nu, \theta)} \right] \left(\frac{\nu}{50 \text{ MHz}} \right)^{-1}, \tag{13}
\end{aligned}$$

where α denotes the angle between shower axis and magnetic field, θ is the shower zenith angle and r_0 is a scale factor of about 110 m. To compare this with our results, we have to convert the experimentally motivated ϵ_ν values to

our theoretically derived $E(\omega)$ values. For the conversion we use the relation

$$\epsilon_\nu = \sqrt{\frac{128}{\pi}} |\vec{E}(\vec{R}, \omega)| \approx 6.4 |\vec{E}(\vec{R}, \omega)| \quad (14)$$

as derived in [5]. The conversion results in

$$\begin{aligned} |\vec{E}(\vec{R}, \omega)| &= 2 \mu\text{V m}^{-1} \text{ MHz}^{-1} \left(\frac{E_p}{10^{17} \text{ eV}} \right) \left(\frac{\sin \alpha \cos \theta}{\sin 45^\circ \cos 30^\circ} \right) \\ &\times \exp \left[\frac{-r}{r_0(\nu, \theta)} \right] \left(\frac{\nu}{50 \text{ MHz}} \right)^{-1}. \end{aligned} \quad (15)$$

Our parametrization yields a value of $3.6 \mu\text{V m}^{-1} \text{ MHz}^{-1}$ for the 50 MHz emission in the center of a 30° zenith angle 10^{17} eV air shower, which is not far off the Allan-value of $2 \mu\text{V m}^{-1} \text{ MHz}^{-1}$. (For comparison, the estimated theoretical limit for a 3σ detection with 1/10/100 LOPES antenna(s) corresponds to $\sim 0.4/0.15/0.05 \mu\text{V m}^{-1} \text{ MHz}^{-1}$, see [5].) The radial dependence in both cases is given by an exponential decay, and the resulting scale-factor in our parametrization indeed corresponds to ~ 110 m for the aforementioned set of parameters. The linear scaling with primary particle energy is identical. Apart from these similarities, there are of course some differences: The frequency dependence in the Allan-formula is specified as ν^{-1} . This is obviously very different from the exponential decay in our parametrization. However, the extrapolated frequency dependence for the Allan-formula rests on rather sparse and uncertain data, some of which lie in the incoherent regime not included in our parametrization. The dependence on shower zenith angle is much more complex than a simple $\cos(\theta)$ trend in our parametrization and is therefore difficult to compare with the Allan-formula. Furthermore, we do not predict any significant dependence of the total field strength on the angle between shower axis and magnetic field (denoted α in the Allan-formula). The emission in an individual linear polarization component, on the other hand, varies with the angle between shower axis and magnetic field axis (cf. eq. (3)).

Overall, our parametrization shows many similarities to the historic Allan-parametrization. The discrepancies, e.g. regarding the frequency dependence, are significant, but considering the sparse experimental data on which the Allan-formula is founded, these discrepancies should not be over-interpreted. In this context one should also remember that later experiments measured significantly lower values for ϵ_ν , a discrepancy that is yet unsolved, but most probably due to calibration issues.

On the one hand, we therefore urgently need new, reliable, well-calibrated experimental data. On the other hand, the modeling efforts have to continue.

In particular, we will improve our simulation by basing it on a more realistic air shower model as given by the CORSIKA code. This will automatically resolve the two major shortcomings of our current model: an unrealistic particle pitch-angle distribution and the assumption of a totally homogeneous air shower development. Taking into account these effects most likely will redistribute flux in such a way that the emission levels in the center region become smaller, making them more consistent with the historical data.

7 Discussion

Our analysis of the Monte Carlo simulation results with regard to the underlying air shower parameters for the first time establishes a number of experimentally relevant features of the radio emission.

One major result is the predicted polarization characteristics of the emission generated in the geomagnetic emission scenario. With this knowledge, polarization-sensitive experiments should be able to directly verify that a major part of the radio emission indeed stems from the geomagnetic mechanism. The overall weak intrinsic asymmetries in the emission pattern (except for those associated to projection effects) on the other hand make experimental setups measuring only the total field strength or one circular polarization component seem less desirable.

Another important insight is provided by the effects arising in air showers with large zenith angles. The intrinsic broadening of the emission pattern associated to the increasing distance of the air shower maximum in combination with projection effects and a flattening of the spectral dependence makes highly inclined air showers an especially interesting target for detection with radio techniques.

Other useful results of our simulations are the predicted wavefront curvature, the expected quasi-linear scaling of the field strengths in the coherent regime, the very weak dependence of the total field strength on the specific geomagnetic field geometry and strength, and the changes to the radial dependence as a function of changing depth of shower maximum.

The successful incorporation of a significant number of air shower and observer parameters into a single parametrization as achieved in this work demonstrates that the emission is overall “well-behaved” and yields a well-interpretable signal. As a solid estimate, the parametrization can be a useful tool for the interpretation of experimental data and the planning of experimental setups. Additionally, there are remarkable similarities between the parametrization of our Monte Carlo results and the historic Allan-formula, although significant

uncertainty regarding the absolute calibration of the historical data remains.

Our current results represent the most sophisticated simulation of radio emission from cosmic ray air showers carried out to date. In the future, we will switch from analytic parametrizations of air shower characteristics as the basis of our simulations to a full-fledged air shower model based on the CORSIKA simulation code, further improving the modeling accuracy. The two main drawbacks of the current model, an over-simplified particle pitch-angle distribution and the disregard of inhomogeneities in the air shower development, will then automatically be resolved.

8 Conclusions

This work presents the cumulative result of our effort at a realistic modeling of the radio emission from cosmic ray air showers in the scheme of coherent geosynchrotron radiation. For the first time, we now have a solid understanding and a quantitative description of the important emission characteristics and their dependences on important air shower and observer parameters. In particular, the emission pattern, spectral dependence, polarization characteristics, primary particle energy dependence, magnetic field dependence and the dependence on air shower geometry and depth of shower maximum for geosynchrotron emission are now theoretically determined. This information is imperative for the interpretation and planning of concrete experiments. In the near future, on the other hand, experiments such as LOPES will provide well-calibrated, reliable data that will allow a direct comparison with our theoretical predictions for the first time. A direct verification of the geomagnetic emission mechanism will then be possible.

Having reached this milestone in the modeling of radio emission from cosmic ray air showers, the next step will be to interface our code with CORSIKA [11], delivering a full-fledged realistic Monte Carlo simulation of radio emission from cosmic ray air showers. Additionally, we wish to incorporate further possible emission mechanisms such as Askaryan-type Čerenkov radiation in our model.

Acknowledgements

We would like to thank Elmar Körding and Andreas Horneffer for the insights and ideas they provided in numerous discussions. T. Huege was supported for this research through a stipend from the International Max Planck Research School (IMPRS) for Radio and Infrared Astronomy at the University of Bonn. LOPES is supported by the German Federal Ministry of Education and

Research under grant No. 05 CS1ERA/1 (Verbundforschung Astroteilchenphysik).

References

- [1] G. A. Askaryan, Soviet Phys. JETP 14 (1962) 441.
- [2] G. A. Askaryan, Soviet Phys. JETP 21 (1965) 658.
- [3] J. V. Jelley, J. H. Fruin, N. A. Porter, T. C. Weekes, F. G. Smith, R. A. Porter, Nature 205 (1965) 327.
- [4] H. Falcke, P. W. Gorham, Detecting radio emission from cosmic ray air showers and neutrinos with a digital radio telescope, *Astropart. Physics* 19 (2003) 477–494.
- [5] T. Huege, H. Falcke, Radio emission from cosmic ray air showers. coherent geosynchrotron radiation, *A&A* 412 (2003) 19–34.
- [6] A. Horneffer, T. Antoni, W. D. Apel, F. Badea, K. Bekk, A. Bercuci, M. Bertaina, et al., Lopes: detecting radio emission from cosmic ray air showers, in: *Astronomical Telescopes and Instrumentation 2004: Gravitational Wave and Particle Astrophysics Detectors*, Proceedings of the SPIE, Vol. 5500, 2004, p. 129.
- [7] A. Belletoile, D. Ardouin, D. Charrier, R. Dallier, L. Denis, P. Eschstruth, T. Gousset, F. Haddad, P. Lautridou, A. Lecacheux, D. Monnier-Ragaigne, A. Rahmani, O. Ravel, Radio detection of cosmic ray extensive air showers: present status of the codalema experiment, in: *Proc. of the SF2A 2004*, 2004, astro-ph/0409039.
- [8] D. A. Suprun, P. W. Gorham, J. L. Rosner, Synchrotron radiation at radio frequencies from cosmic ray air showers, *Astropart. Physics* 20 (2003) 157–168.
- [9] T. Gousset, O. Ravel, C. Roy, Are vertical cosmic rays the most suitable to radio detection ?, Vol. submitted, 2004, astro-ph/0402426.
- [10] T. Huege, H. Falcke, Radio emission from cosmic ray air showers: Monte carlo simulations, *A&A* In press, astro-ph/0409223.
- [11] D. Heck, J. Knapp, J. N. Capdevielle, G. Schatz, T. Thouw, Corsika: A monte carlo code to simulate extensive air showers, Forschungszentrum Karlsruhe Report FZKA 6019.
- [12] C. L. Pryke, A comparative study of the depth of maximum of simulated air shower longitudinal profiles, *Astropart. Physics* 14 (2001) 319–328.
- [13] J. Knapp, D. Heck, S. J. Sciutto, M. T. Dova, M. Risse, Extensive air shower simulations at the highest energies, *Astropart. Physics* 19 (2003) 77–99, astro-ph/0206414.
- [14] H. R. Allan, Radio emission from extensive air showers, *Prog. in Element. part. and Cos. Ray Phys.* Vol. 10 (1971) 171.